# Optimal Powertrain Energy Management for Autonomous Hybrid Electric Vehicles with Flexible Driveline Power Demand Using Approximate Dynamic Programming

Mohammadali Kargar, *Student Member, IEEE,* Tohid Sardarmehni, Xingyong Song, *Member, IEEE*

***Abstract*—The increasing number of vehicles, the excessive use of fossil fuels, and the related safety and environmental issues have motivated studies on autonomous vehicles and Hybrid Electric Vehicles (HEVs). In this work, we focus on the control of the powertrain energy management for an autonomous HEV. A new powertrain control strategy is enabled by leveraging one of the uniqueness in the powertrain management of an autonomous vehicle, i.e., the instantaneous power generated by the powertrain does not need to exactly follow the power demand by the vehicle motion controller. This is referred to as *flexible power demand*, which adds an extra degree of freedom to the powertrain energy management, and can lead to control design achieving better fuel economy. The powertrain control is then formulated under the Approximate Dynamic Programming (ADP) framework, and the power flexibility is incorporated in the ADP formulation. At last, an example of multiple connected HEVs following a leader vehicle operating in an off-road scenario is given to demonstrate the feasibility of the proposed method.**

***Index Terms*—Autonomous Vehicles, Hybrid Electric Vehicles, Powertrain Energy Management.**

## I. Introduction

THE increasing electrification and autonomy are two recent trends in the automotive industry. Hybridization is an intermediate step on the path toward full electrification aimed to make electric vehicles more competitive against conventional vehicles with Internal Combustion Engines (ICEs) [1]. A hybrid vehicle is a system powered by multiple power sources, usually an ICE and a battery pack. The potential in reducing fuel consumption and emissions enabled by having an extra degree of freedom in the HEV's powertrain has drawn research attention over the last two decades [2]–[11]. The existence of an additional power source in HEVs necessitates a control strategy to split power between these power sources optimally, known as powertrain energy management [12]. A number of methodologies have been proposed for development of such control strategies ranging from Dynamic Programming (DP) [13], [14] to rule-based [15], [16], equivalent consumption minimization strategy [17], [18], fuzzy logic [19], [20], model predictive control [21], [22], and reinforcement learning [23], [24]. Powertrain energy management is a critical issue since improper power split management will cause battery to overcharge or drain, not satisfy the required power demand, and decrease the power efficiency.

Meanwhile, research on autonomous vehicles has gained momentum recently. Its combination with powertrain hybridization results in an autonomous HEV. An autonomous HEV has two levels of control (Fig. 1) [25]. In the upper level (vehicle level), the controller optimizes external dynamics of the vehicle, including position and velocity profiles, to satisfy predefined maneuvering goals. The power needed in the driveline is determined at this level. In the lower level (powertrain level), the controller shall decide how to split the power demand among different power supplies efficiently to achieve optimal fuel economy. Most existing research studies these two levels separately: some [26]–[31] have only focused on the upper-level control design, while others [32]–[37] have solely studied the powertrain-level control strategies. However, studies have shown that augmenting these two levels offers increased opportunities to enhance fuel economy by more than 30% [25], [38].

The benefits of joint optimization of these two trends have urged the researchers to focus on solving motion control and power energy management in a unified framework [39]–[45]. While it is possible to integrate the two levels of controllers as a single controller, the design of such an integrated controller can be complicated due to the coupled augmented vehicle and powertrain dynamics [25]. Also, real-time optimization of high-order dynamics can be challenging. To mitigate computational burden due to high coupling between dynamics of the upper level and lower level, [46]–[48] proposed a hierarchical control



M. Kargar is with the Department of Mechanical Engineering, College of Engineering, Texas A&M University, College Station, TX 77843, USA. (e-mail: mohammadkrg@tamu.edu).

T. Sardarmehni is with the Department of Mechanical Engineering, California State University Northridge, Northridge, CA 91330, USA. (email: t.sardarmehni@gmail.com).

X. Song is with the Department of Engineering Technology and Industrial Distribution, the Department of Mechanical Engineering, and the Department of Electrical and Computer Engineering, College of Engineering, Texas A&M University, College Station, TX 77843, USA. (e-mail: songxy@tamu.edu).

Manuscript received mm dd, 20XX.

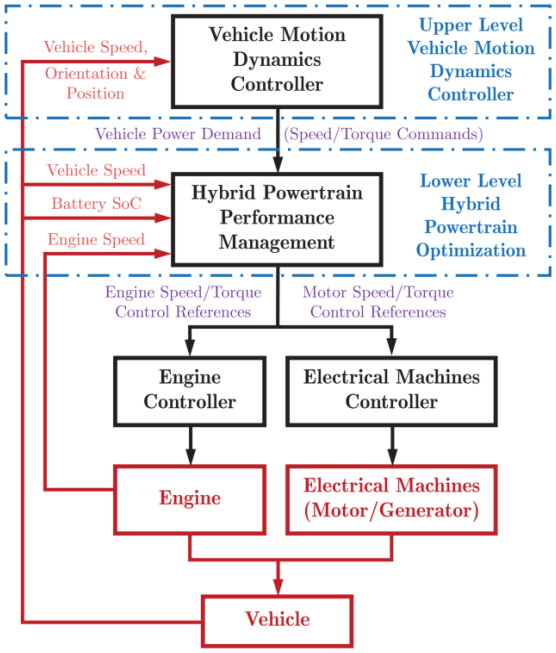


Fig. 1. Two Levels of Control for Autonomous HEVs [25].

framework to optimize (1) the vehicle's speed profile, and (2) powertrain efficiency of the vehicle for the optimal speed profile derived in (1). Although these studies have shown promising results, these two levels are still solved separately, and the full potential of integrated optimization in fuel minimization is still unleashed.

Recently, some researchers have applied the emerging idea of flexible power/torque request [25], [49]. This approach leverages the uniqueness of powertrain management in an autonomous vehicle, i.e., the lower-level controller does not need to exactly meet the power required by the upper level at every moment. Note that the power demand in the upper-level controller is determined without considering the internal powertrain dynamics; thus, the power demand requested by the upper level may not be in favor of powertrain management. Giving flexibility to powertrain management can potentially lead to a more efficient hybrid power split strategy. In this strategy, the two control levels are still implemented separately, and the power demand from the vehicle-level control is given to the powertrain-level control. Nevertheless, instead of strictly following this power demand, the powertrain-level controller is allowed to have a certain amount of flexibility in the instantaneous power provided (Fig. 2), while the vehicle still satisfies the maneuver goals set by the upper-level controller as time reaches a specified time horizon. This can lead to a better fuel economy since the powertrain-level controller will have more flexibility to have the power sources operating in the most efficient condition. This strategy is not applicable in conventional vehicles driven by humans, as it would conflict with the driver's intentions if the lower-level controller supplies a power less/more than what the driver has intended.

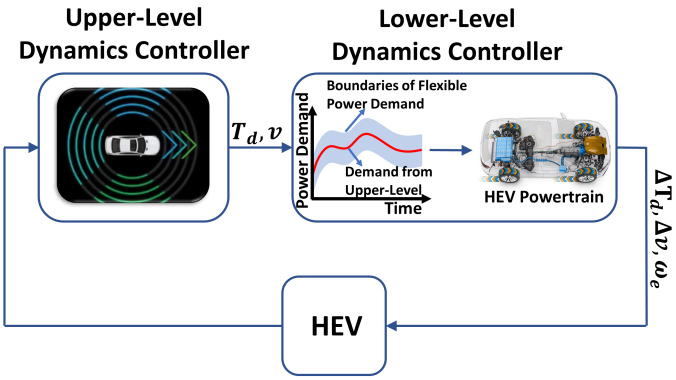


Fig. 2. Energy Management Hierarchy with Flexible Power Demand.

However, it is possible to be implemented for autonomous vehicles, since both vehicle and powertrain controllers operate in the background.

Nevertheless, methods used in existing works related to powertrain control with flexible power demand make them less practical in the application of HEV power management. [49] proposed an adaptive strategy to optimize power splits for an autonomous parallel HEV with flexible power demand. However, the main drawback in [49] is that the proposed method does not guarantee that the vehicle reaches the destination set by the upper-level controller at the end of the time horizon considered. Also, in [25], Pontryagin's Minimum Principle (PMP) was deployed to optimize the powertrain control optimization. PMP is a powerful method in addressing powertrain energy management for conventional HEVs. Nevertheless, when state limitations are included in the definition of the problem, it can be challenging to implement PMP to handle them [50]–[52]. Thus, it can lead to some convergence issues when dealing with powertrain management for autonomous HEVs with flexible driveline power demand wherein state constraints shall be enforced [25]. In addition, PMP mainly provides an open-loop solution dependent on the initial conditions [53]. Thus, each time the initial condition changes, a new optimization is required. Also, trial-and-error is necessary to set the initial profile of control inputs given to the shooting method [54] used for PMP [55].

To address these challenges, in this paper, ADP is adopted to solve the powertrain energy management optimization with flexible power demand for the first time. ADP is a computationally efficient nonlinear optimal control method that learns the optimal behavior of a system using reinforcement learning. In ADP, the dynamical states are incorporated into the controller through the neural network, which makes ADP a closed-loop control solution. Thus, once the controllers are trained, they can be used for a wide range of initial conditions within the region in which the controllers have been trained. In this paper, the powertrain control problem and the flexibility of the power demand are specifically formulated to accommo-

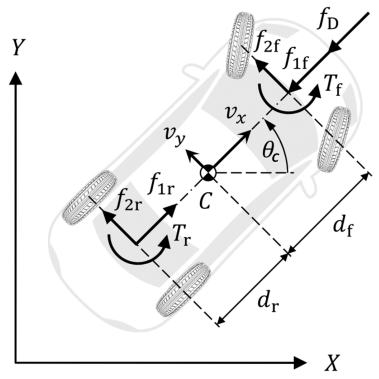


Fig. 3. Free Body Diagram of a Vehicle [25].

date the setup needed in the ADP solver. For example, the non-affine nonlinear powertrain dynamics are converted to an affine form so the ADP can be efficiently implemented. The control performance is shown to demonstrate its fuel-saving benefit.

The outline of this paper is as follows. In Section II, the vehicle-level's dynamics and control are discussed. Section III presents the energy management in an HEV and the incorporation of power flexibility into its formulation. State Space model and ADP framework are introduced in Section IV followed by a numerical example in Section V. At last, concluding remarks are given in Section VI.

## II. Vehicle-Level Dynamics and Control

Consider a typical autonomous rear-wheel-drive vehicle. To relax the complexities, the effective forces on the rear side and front side are summed up at their corresponding mid-axles. Fig. 3 shows the free body diagram. X and Y consist of an inertial reference frame in which the variables $X_C, Y_C, \theta_C$ show the horizontal and vertical position of the vehicle's mass center $C$ in the frame and its orientation, respectively. The kinematics of the vehicle can be written as below [25]:

$$\dot{X}_C = v_x(t)cos(\theta_C(t)) - d_r\omega(t)sin(\theta_C(t)), X_C(0) = X_{C,0} \tag{1}$$

$$\dot{Y}_C = v_x(t)sin(\theta_C(t)) + d_r\omega(t)cos(\theta_C(t)), Y_C(0) = Y_{C,0} \tag{2}$$

$$\dot{\theta}_C = \omega(t), \qquad \theta_C(0) = \theta_{C,0} \tag{3}$$

where, $v_x$ is the longitudinal velocity, $\omega$ is the yaw angular velocity of the vehicle, and $d_r$ is the distance between the center of mass $C$ and the rear axle. Besides, the dynamics of the vehicle are as follows [25]:

$$\bar{m}\dot{v}_x(t) = \alpha m d_r\omega^2(t) - \frac{1}{2}\rho C_{drag}A_f v_x^2(t) - f_\mu mg + \frac{1}{r}T_d(t) - \frac{\alpha(d_f+d_r)}{d_f}\frac{\omega(t)}{v_x(t)}T_s(t), v_x(0) = v_{x,0} \tag{4}$$

$$\bar{I}\dot{\omega}(t) = -md_r\omega v_x(t) + \frac{(d_f+f_r)}{d_r}T_s(t), \quad \omega(0) = \omega_0 \tag{5}$$

where $\bar{m} = m + \frac{I_f+I_r}{r^2}$, $\bar{I} = I + md_r^2$, $\alpha = 1 + \frac{I_f(d_f+d_r)^2}{Ir^2}$, $m$ is the total mass of the vehicle, and $I$ is the yaw inertia moment. $I_r$ denotes the equivalent moment of inertia of the rear wheels and the rear axle plus all internal rotary components translated at the rear axle about the axis of the rear axle. $I_f$ denotes the equivalent moment of inertia of the front wheels and front axle about the axis of the front axle when the steering angle is zero. $d_f$ is the distance between the center of mass $C$ and the front axle, and $r$ is the radius of the wheels. $T_d$ and $T_s$ are the driving and steering torques, respectively. $A_f$, $\rho$, $C_{drag}$, and $f_\mu$ are the frontal area of the vehicle, the air density, the drag coefficient, and the rolling resistance coefficient, respectively. The control design for this system is a classic problem and hence not covered in this paper. Interested readers are referred to [56] for more details. After designing the upper-level controller, one may find the current and the future trajectory information of the vehicle plus steering and driving torques needed for the vehicle to stay on the predicted path using traffic data from connected vehicles nearby and the transportation infrastructures. Prediction of the future trajectory using real-time traffic information has drawn extensive attention in recent years [57], [58]. Hence, the authors' focus is more on powertrain energy management optimization and fuel consumption based on the generated driveline torque demands from the upper-level controller.

## III. Energy Management in Power-Split Hybrid Electric Powertrain

### A. Defining the concept of flexibilities

The driveline power and torque demands obtained from the upper level are used in the lower-level controller. The controller is in charge of deciding how to supply the driveline power demand from the ICE and the electrical machinery. In the majority of the research conducted in the field of hybrid powertrain energy management, the convention is to strictly follow the power demand determined from the vehicle-level controller and try to optimize the powertrain based on that [33], [35], [36]. To take advantage of the uniqueness of powertrain energy management for autonomous vehicles, in this paper, we allow flexibility in the instantaneous power supplied by the powertrain. This introduces an extra degree of freedom in the powertrain control optimization which can further improve fuel efficiency.

Considering the demand from the upper-level controller as a reference, certain ranges of deviation are admissible in instantaneous driveline power demand. Although this will result in deviation in the desired vehicle speed and displacement, this deviation will only happen in the intermediate time steps, and the final vehicle displacement and velocity in each considered time horizon will be met. In other words, it means that the longitudinal position and velocity plus driveline torque demand might be different from the baseline at each intermediate time step, but the deviation in the longitudinal position and velocity must vanish as time reaches the time horizon.

Let $\Delta x \triangleq \tilde{x} - x$ be deviations of the longitudinal position of the vehicle where $x$ denotes the baseline longitudinal displacement obtained from the upper-level controller, and $\tilde{x}$ denotes the flexible longitudinal displacement. Also, define $\Delta v_x \triangleq \tilde{v}_x - v_x$ to be deviations of the longitudinal velocity of the vehicle where $\tilde{v}_x$ denotes the flexible longitudinal velocity. Rewriting the external dynamics of the vehicle considering the abovementioned flexibilities yields:

$$\bar{m}\dot{\tilde{v}}_x(t) = \alpha m d_r \tilde{\omega}^2(t) - \frac{1}{2}\rho C_{drag} A_f \tilde{v}_x^2(t) - f_\mu mg + \frac{1}{r}\tilde{T}_d(t) - \frac{\alpha(d_f + d_r)}{d_f}\frac{\tilde{\omega}(t)}{\tilde{v}_x(t)}\tilde{T}_s(t), \quad \tilde{v}_x(0) = \tilde{v}_{x,0} \tag{6}$$

where $\tilde{\omega}$ is the flexible yaw angular velocity and $\tilde{T}_s$ and $\tilde{T}_d$ are the flexible steering and driveline torques, respectively.

**Assumption 1.** *The generated vehicle-level trajectory is smooth enough such that one can neglect the effect of the yaw angular velocity of the vehicle on its longitudinal dynamics, i.e., $\omega(t) \approx \tilde{\omega}(t) \approx 0$ [59], [60].*

Subtracting (4) from (6) followed by a division by $\bar{m}$ yields:

$$\Delta\dot{v}_x(t) = \dot{\tilde{v}}_x(t) - \dot{v}_x(t) = \frac{1}{\bar{m}}[-\frac{1}{2}\rho C_{drag} A_f \Delta v_x(t)(2v_x(t) + \Delta v_x(t)) + \frac{1}{r}\Delta T_d(t)], \qquad \Delta v_x(0) = 0. \tag{7}$$

Note that:

$$\tilde{v}_x^2(t) - v_x^2(t) = (\tilde{v}_x(t) + v_x(t))(\tilde{v}_x(t) - v_x(t)) = \Delta v_x(t)(2v_x(t) + \Delta v_x(t)). \tag{8}$$

Also, $\Delta v_x(0) = 0$ comes from the fact that at the beginning of the driving cycle, the lower-level controller starts with the same longitudinal velocity resulting from the vehicle level. In addition, $\Delta T_d \triangleq \tilde{T}_d - T_d$ serves as the control input. Accordingly, the rate of change in the longitudinal position deviation is as follows:

$$\Delta\dot{x}(t) = \Delta v_x(t), \qquad \Delta x(0) = 0. \tag{9}$$

Similarly, $\Delta x(0) = 0$ comes from the fact that at the beginning, $\tilde{x}(0) = x(0)$.

### B. Powertrain Dynamics

Consider a typical power-split HEV powertrain shown in Fig. 4. This mechanism, which Toyota introduced for Prius vehicles, is made up of two gear sets, a planetary and a coupler one, a battery, an inverter, and two electrical machines which can serve as a generator or a motor. In the literature, the one that is usually operating as an electricity generation unit is called "generator", and the one that mostly acts as a motion power output is labeled as "motor." The planetary gear set consists of three parts: sun, carrier, and ring. Here, the sun is connected to the generator, and the carrier is linked to the engine. G0 connects the ring's shaft and the electric motor's shaft through two identical gears G1 and G2 together to drive the driveline. Neglecting the inertia of the moving parts in the powertrain, one can find the following algebraic equations between different components using the power balance at the planetary gear set:

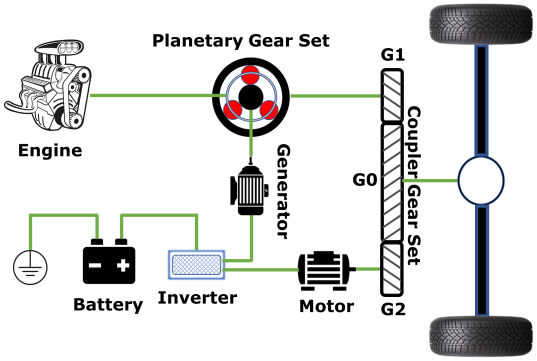


Fig. 4. Toyota Prius Powertrain Schematic.

$$T_g(t) = -(\frac{r_s}{r_s + r_r})T_e(t) \tag{10}$$

$$\omega_e(t) = (\frac{r_r}{r_s + r_r})\omega_r(t) + (\frac{r_s}{r_s + r_r})\omega_g(t) \tag{11}$$

where $T_g$ and $T_e$ denote the generator's torque and the engine's torque, respectively. $r_s$ and $r_r$ are the radii of the sun gear and the ring gear, respectively. $\omega_e$ is the engine's angular velocity, and $\omega_r$ and $\omega_g$ are the corresponding angular velocity of the ring and the generator, respectively. Similarly, the power balance in the coupler gear set yields the following algebraic equations:

$$T_m(t) = \frac{1}{k_C}\tilde{T}_d(t) - (\frac{r_r}{r_s + r_r})T_e(t) \tag{12}$$

$$\omega_m(t) = k_C\frac{\tilde{v}_x(t)}{r} = k_C\tilde{\omega}_d(t) \tag{13}$$

where $T_m$ is the motor's torque. $\tilde{\omega}_d$ is the angular driveline velocity. Also, $k_C$ is the gear ratio at the coupler gear set. Note that $(\frac{r_r}{r_s+r_r})T_e(t)$ is equal to the ring's torque output from the planetary gear set. In addition, as G1 and G2 are identical, it is clear that their angular speeds are the same since both are attached to G0, hence:

$$\omega_r(t) = \omega_m(t) \tag{14}$$

where $\omega_m$ represents the motor's angular velocity. Rewriting (11) yields:

$$\omega_e(t) = (\frac{r_r}{r_s + r_r})\omega_m(t) + (\frac{r_s}{r_s + r_r})\omega_g(t) \tag{15}$$

*Remark* 1. Usually, in a real power-split HEV powertrain, the motor is connected directly to the ring without the help of any coupler gear set. The coupler gear set is just added here to simplify the demonstration of how the powertrain drives the vehicle, and it does not change any of the relations in the real case as G1 and G2 are assumed to be identical.

Finally, by considering the power balance at the inverter, the algebraic equation is:

$$P_{batt}(t) = P_m(t)+P_g(t) = \mu_m^{k_m} T_m(t)\omega_m(t)+\mu_g^{k_g} T_g(t)\omega_g(t) \tag{16}$$

where $P_{batt}$, $P_m$, and $P_g$ denote the battery power, the motor power, and the generator power, respectively. Conventionally in electrical machines, a negative power shows the machine is operating as a generator while a positive power shows it is functioning as a motor, and both $P_m$ and $P_g$ can be positive or negative based on their function. $\mu_m$ and $\mu_g$ represent the efficiency coefficients of the motor and the generator when they are generating electricity, respectively, and they vary between (0,1). As a result of mechanical and electrical energy loss, when electrical machines are functioning as an electric motor, the battery is discharged more than what is delivered at the output shaft. When they are functioning as a generator, the battery is charged less than what is produced by them. Hence, $k_m$ and $k_g$ are equal to 1 if their corresponding electrical machines function as generators and equal to -1 when they function as motors. Also, notice that a negative $P_{batt}$ means the battery is charging while a positive $P_{batt}$ shows it is discharging. Using (10) to (16), $P_{batt}$ is formulated as:

$$\begin{aligned} P_{batt}(t) =& \mu_m^{k_m}\tilde{T}_d(t)\tilde{\omega}_d(t) - \mu_g^{k_g} T_e(t)\omega_e(t) \\ &- \frac{k_c r_r(\mu_m^{k_m} - \mu_g^{k_g})}{r_s + r_r} T_e(t)\tilde{\omega}_d(t). \end{aligned} \tag{17}$$

The dynamics of the battery are as follows [61]:

$$\begin{aligned} \dot{SoC}(t) = -\frac{V_{batt} - \sqrt{V_{batt}^2 - 4R_{batt}P_{batt}(t)}}{2R_{batt}Q_{batt}}, \\ SoC(0) = SoC_0 \end{aligned} \tag{18}$$

where $SoC$ is the state of the charge of the battery. Also, $V_{batt}$, $R_{batt}$, and $Q_{batt}$ represent the battery's open-circuit voltage, internal resistance, and capacitance, respectively.

## IV. Solving Optimal Energy Management with ADP

### A. State-Space Model

In this section, the State-Space representation is discussed. Considering (7), (9), (17), and (18), the system dynamics can be summarized as below:

$$\dot{\mathbf{X}}(t) = \mathbf{F}(\mathbf{X}(t), \mathbf{U}(t)), \qquad \mathbf{X}(0) = \mathbf{X}_0 \tag{19}$$

where the state vector $\mathbf{X}(t)$, the input vector $\mathbf{U}(t)$, and the non-affine nonlinear function $\mathbf{F}$ are defined as:

$$\mathbf{X}(t) \triangleq [\Delta x(t), \Delta v_x(t), SoC(t)]^T \tag{20}$$

$$\mathbf{U}(t) \triangleq [\Delta T_d(t), \omega_e(t), T_e(t)]^T \tag{21}$$

$$\begin{aligned} \mathbf{F} = \Bigg[ \Delta v_x(t), \frac{1}{\tilde{m}}[-\frac{1}{2}\rho C_{drag} A_f \Delta v_x(t)(2v_x(t) + \Delta v_x(t)) + \\ \frac{1}{r}\Delta T_d(t)], -\frac{V_{batt} - \sqrt{V_{batt}^2 - 4R_{batt}P_{batt}(t)}}{2R_{batt}Q_{batt}} \Bigg]^T. \end{aligned} \tag{22}$$

**Assumption 2.** *In the study of the power-split HEVs, given the two degrees of freedom feature of the powertrain, one can assume that for any engine power $P_e(t) = T_e(t)\omega_e(t)$, the solution pair $(T_e(t), \omega_e(t))$ will be such that the engine power lies on the most efficient fuel consumption curve shown on the engine map [25].*

The engine map used in this study is shown in Fig. 5. It is visible that on the most efficient fuel consumption curve, for any specific engine power possible, i.e., $0 \leq P_e(t) \leq P_{e,max}$, a smooth 1-to-1 correspondence exists between the engine's angular velocity and the engine's torque. To reduce the number of inputs and hence, reduce the complexities in solving the optimization problem, $T_e(t)$ can be replaced by a function of $\omega_e(t)$.

$$T_e(t) \propto \omega_e(t) \rightarrow T_e(t) = h_1(\omega_e(t)) \tag{23}$$

where $h_1 : \mathbb{R}_+ \rightarrow \mathbb{R}_+$ in which $\mathbb{R}_+$ is the set of nonnegative real numbers. Also, note that fuel consumption which is a function of $T_e(t)$ & $\omega_e(t)$, now can be estimated by $\omega_e(t)$ alone:

$$\dot{m}_{fuel}(t) \propto \omega_e(t) \rightarrow \dot{m}_{fuel}(t) = h_2(\omega_e(t)) \tag{24}$$

where $h_2 : \mathbb{R}_+ \rightarrow \mathbb{R}_+$. Therefore, with **Assumption 2**, the vector of inputs will be replaced by $\mathbf{U}(t) = [\Delta T_d(t), \omega_e(t)]^T$.

*Remark* 2. Under Assumption 2 and using Eq. (23), for any given $\omega_e$, its corresponding $T_e$ is found by using the engine map, and thus, the engine torque limit is met.

### B. Input Affine Transformation and System Nondimensionalization

To apply the ADP method in [62], the system needs to be in a control affine form. However, the inputs, $\omega_e$ and $\Delta T_d$, appear nonlinearly in Eq. (18) through $P_{batt}(t)$, which makes the powertrain system dynamics be non-affine. Thus, the system dynamics need to be first transformed. Similar to the method used in [63], a transformation is applied such that the inputs are taken as the new

$$\begin{bmatrix} \dot{x}_1(t) \\ \dot{x}_2(t) \\ \dot{x}_3(t) \\ \dot{x}_4(t) \\ \dot{x}_5(t) \end{bmatrix} = \begin{bmatrix} x_2(t) \\ \frac{1}{\tilde{m}}\left[-\frac{1}{2}\rho C_{drag} A_f x_2(t)(2v_x(t) + x_2(t)) + \frac{1}{r}(x_4(t))\right] \\ -\frac{V_{batt} - \sqrt{V_{batt}^2 - 4R_{batt}P_{batt}(t)}}{2R_{batt}Q_{batt}} \\ 0 \\ 0 \end{bmatrix} + \begin{bmatrix} 0 & 0 \\ 0 & 0 \\ 0 & 0 \\ 1 & 0 \\ 0 & 1 \end{bmatrix} \begin{bmatrix} u_1(t) \\ u_2(t) \end{bmatrix} \tag{27}$$

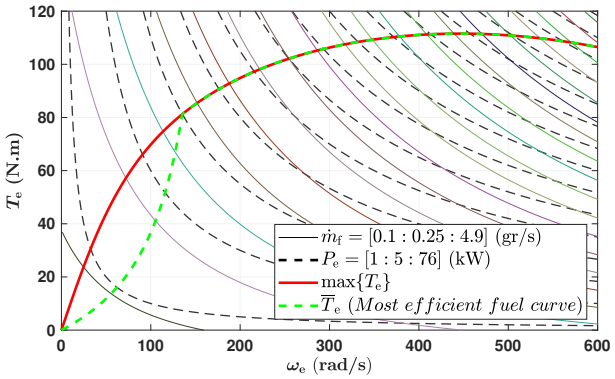


Fig. 5. Engine Map.

states, and their derivatives are taken as the new inputs. This shifts the nonlinearity of the original inputs to be states in the newly transformed system, and have the new inputs appear in the transformed dynamics in an affine fashion. The new state vector and input vector are:

$$\mathbf{X}_{New}(t) = [\Delta x(t), \Delta v_x(t), SoC(t), \Delta T_d(t), \omega_e(t)]^T \quad (25)$$

$$\mathbf{U}_{New}(t) = [\Delta \dot{T}_d(t), \dot{\omega}_e(t)]^T. \quad (26)$$

Eq. (27) shows the transformed input-affine system dynamics, in which to simplify the notation, $\Delta x, \Delta v_x, SoC, \Delta T_d$, and $\omega_e$ are referred to as $x_1, x_2, x_3, x_4$, and $x_5$, respectively. In a similar manner, $\Delta \dot{T}_d$, and $\dot{\omega}_e$ are referred to as $u_1$, and $u_2$, respectively.

Also, note that each state varies between different ranges. For instance, $x_1$ is expected to vary between zero and hundreds of meters, while $x_2$ is expected to vary between zero and tens of meters per second. Thus, Eq. (28) is used to nondimensionalize the system prior to the training, to make states vary between [-1, +1] and help the training process.

$$\bar{x}_i = \frac{x_i}{X_{max,i}}, i = 1, 2, ..., 5 \quad (28)$$

where $\bar{x}_i$, and $X_{max,i}$ denote the $ith$ nondimensionalized state, and the maximum absolute value of $x_i$, respectively. This will convert the system dynamics to Eq. (29).

### C. Solving Optimal Control Problem Using ADP

For simplicity of derivation, Eq. (29) is referred as:

$$\dot{\mathbf{x}}(t) = f_c(\mathbf{x}(t)) + g_c(\mathbf{x}(t))\mathbf{u}(t), \qquad \mathbf{x}(0) = \mathbf{x}_0 \quad (30)$$

where $\mathbf{x}(t) \in \mathbb{R}^n$ is the state vector, and smooth functions $f_c : \mathbb{R}^n \to \mathbb{R}^n$ and $g_c : \mathbb{R}^{n\times m}$ represent the dynamics of the system. Also, $\mathbf{u}(t) \in \mathbb{R}^m$ is the input vector. Given the initial conditions $\mathbf{x}(0) = \mathbf{x}_0 \in \mathbb{R}^n$, the cost function is defined as below:

$$J_c = \frac{1}{2}\int_0^{t_f} \mathbf{x}(t)^T Q_c \mathbf{x}(t) + \mathbf{u}(t)^T R_c \mathbf{u}(t)\ dt + \psi(\mathbf{x}(t_f)) \quad (31)$$

where $t_f$ is the final time. Matrices $Q_c \in \mathbb{S}_+^{n\times n}$ and $R \in \mathbb{S}_{++}^{m\times m}$put penalties on the intermediate states $\mathbf{x}(t)$ and inputs $\mathbf{u}(t)$ $(t \neq t_f)$. $\mathbb{S}_+^{k\times k}$ and $\mathbb{S}_{++}^{k\times k}$ denote the sets of $k \times k$ positive semi-definite and positive definite matrices, respectively. $\psi : \mathbb{R}^n \to \mathbb{R}$ puts a penalty on the terminal states, and is used to ensure that the system will reach the desired terminal point $x_{des}(t_f)$. $\psi$ can be defined in a quadratic form as:

$$\psi(\mathbf{x}(t_f)) = \frac{1}{2}(\mathbf{x}_{t_f} - \mathbf{x}_{des}(t_f))^T S(\mathbf{x}_{t_f} - \mathbf{x}_{des}(t_f)) \quad (32)$$

where $S \in \mathbb{S}_{++}^{n\times n}$. Let $\delta t$ be a small enough sampling time, one can discretize (30)-(32) by using the Euler method as:

$$\mathbf{x}_{k+1} = f(\mathbf{x}_k) + g(\mathbf{x}_k)\mathbf{u}_k, \qquad k = 0, 1, 2, ..., N-1 \quad (33)$$

$$J = \frac{1}{2}\sum_{k=0}^{N-1} \mathbf{x}_k^T Q \mathbf{x}_k + \mathbf{u}_k^T R \mathbf{u}_k + \frac{1}{2}(\mathbf{x}_N - \mathbf{x}_{des}(N))^T S(\mathbf{x}_N - \mathbf{x}_{des}(N)) \quad (34)$$

where $k$ is the discrete time index, $N \triangleq \frac{t_f}{\delta t}$ is the total number of time steps. $\mathbf{x}_k$, and $\mathbf{u}_k$ denote the state and the input vectors at time step $k$, respectively. Also, $f(\mathbf{x}_k) = \mathbf{x}_k + \delta t f_c(\mathbf{x}_k)$, $g(\mathbf{x}_k) = \delta t g_c(\mathbf{x}_k)$, $Q = \delta t Q_c$, and $R = \delta t R_c$.

The cost-to-go $J(\mathbf{x}_k, k)$ is defined as the cost from $\mathbf{x}_k$ at time step $k$ to the end of the time horizon and is equal to:

$$\begin{aligned} J(\mathbf{x}_k, k) &= \frac{1}{2}\sum_{\tau=k}^{N-1} \mathbf{x}_\tau^T Q \mathbf{x}_\tau + \mathbf{u}_\tau^T R \mathbf{u}_\tau \\ &\quad + \frac{1}{2}(\mathbf{x}_N - \mathbf{x}_{des}(N))^T S(\mathbf{x}_N - \mathbf{x}_{des}(N)) \\ &= \frac{1}{2}\mathbf{x}_k^T Q \mathbf{x}_k + \mathbf{u}_k^T R \mathbf{u}_k + J(\mathbf{x}_{k+1}, k+1), \\ &\qquad k = 0, 1, 2, ..., N-1. \end{aligned} \quad (35)$$

$$\begin{bmatrix} \dot{\bar{x}}_1 \\ \dot{\bar{x}}_2 \\ \dot{\bar{x}}_3 \\ \dot{\bar{x}}_4 \\ \dot{\bar{x}}_5 \end{bmatrix} = \begin{bmatrix} \frac{X_{max,2}}{X_{max,1}}\bar{x}_2 \\ \frac{1}{\bar{m}}\left[-\frac{1}{2}\rho C_{drag} A_f \bar{x}_2(t)(2v_x(t) + X_{max,2}\bar{x}_2(t)) + \frac{1}{rX_{max,2}}(X_{max,4}\bar{x}_4)\right] \\ -\frac{V_{batt} - \sqrt{V_{batt}^2 - 4R_{batt}P_{batt}(t)}}{2R_{batt}Q_{batt}X_{max,3}} \\ 0 \\ 0 \end{bmatrix} + \begin{bmatrix} 0 & 0 \\ 0 & 0 \\ 0 & 0 \\ \frac{1}{X_{max,4}} & 0 \\ 0 & \frac{1}{X_{max,5}} \end{bmatrix} \begin{bmatrix} u_1 \\ u_2 \end{bmatrix} \quad (29)$$

It can be proven that [62] the optimal control input $\mathbf{u}_k^*$ which minimizes $J(\mathbf{x}_k, k)$, can be calculated by:

$$\mathbf{u}_k^* = -R^{-1} g(\mathbf{x}_k)^T \frac{\partial J(\mathbf{x}_{k+1}, k+1)}{\partial \mathbf{x}_{k+1}} = -R^{-1} g(\mathbf{x}_k)^T \boldsymbol{\lambda}_{k+1} \tag{36}$$

where $\boldsymbol{\lambda}_k \triangleq \frac{\partial J(\mathbf{x}_k, k)}{\partial \mathbf{x}_k}$ is the costate vector at time step $k$. Considering (35), it can be shown that:

$$\boldsymbol{\lambda}_k = \frac{\partial J(\mathbf{x}_k, k)}{\partial \mathbf{x}_k} = \begin{cases} S(\mathbf{x}_k - \mathbf{x}_{des}(N)), k = N \\ Q\ \mathbf{x}_k + \frac{\partial \mathbf{x}_{k+1}}{\partial \mathbf{x}_k} \boldsymbol{\lambda}_{k+1}, k = 0, 1, ..., N-1 \end{cases} \tag{37}$$

It can also be shown that [62] a mapping exists between $\boldsymbol{\lambda}_{k+1}$ and $\mathbf{x}_k$, that can be captured by an ADP method called Single Network Adaptive Critic (SNAC) with a closed-form given below:

$$\boldsymbol{\lambda}_{k+1} = W_k^T \Phi(\mathbf{x}_k). \tag{38}$$

In this linear-in-weight neural network, the smooth vector-valued function $\Phi : \mathbb{R}^n \to \mathbb{R}^p$ takes $\mathbf{x}_k$ as the inputs and outputs $p$ linearly independent neurons (also called basis functions). $W_k \in \mathbb{R}^{p \times n}$ is the unknown network's weight matrix at time step $k$. The weight matrix is iteratively solved through the following equations [62]:

$$W_{N-1}^{i+1^T} \Phi(\mathbf{x}_{N-1}) = S\Big(f(\mathbf{x}_{N-1}) - g(\mathbf{x}_{N-1}) R^{-1} g(\mathbf{x}_{N-1})^T \times W_{N-1}^{i^T} \Phi(\mathbf{x}_{N-1}) - \mathbf{x}_{des}(N)\Big) \tag{39}$$

$$W_k^{i+1^T} \Phi(\mathbf{x}_k) = Q\Big(f(\mathbf{x}_k) - g(\mathbf{x}_k) R^{-1} g(\mathbf{x}_k)^T W_k^{i^T} \Phi(\mathbf{x}_k)\Big) + (\frac{\partial \mathbf{x}_{k+2}}{\partial \mathbf{x}_{k+1}})^T W_{k+1}^T \Phi\Big(f(\mathbf{x}_k) - g(\mathbf{x}_k) R^{-1} g(\mathbf{x}_k)^T W_k^{i^T} \Phi(\mathbf{x}_k)\Big) \quad k = 0, 1, 2, ..., N-2 \tag{40}$$

Once the weight matrix is obtained, $\boldsymbol{\lambda}_k$ and the optimal control input $\mathbf{u}_k^*$ can be found from Eqs. (38) and (36). The training algorithm is detailed in Algorithm 1.

*Remark* 3. As proved in [62], the iterations given in Eqs. (39) and (40) are contraction mappings, meaning that, starting from any finite initial guess on $W_k^0$, k={0,1,...N-1}, they converge to the fixed point solution of the iterations. In algorithm 1, the network weights $W_k^0$ are initialized to zero. Also, to compute the norm of the difference between two successive iterative weight matrices in steps (7) and (15), mean absolute error performance is used. For more details, refer to [62].

*Remark* 4. In Algorithm 1, if the battery power is out of the limit for a sample in any step of training, the searching-based ADP process will discard that sample from the set of training samples before training the corresponding neural network in steps 6 and 14.

*Remark* 5. Eqs. (36) and (38) yield that $\mathbf{u}_k^*$ can be calculated by having $R, g(\mathbf{x}_k), W_k, and\ \Phi(\mathbf{x}_k)$. Thus, after the convergence of the weights using Algorithm 1, the optimal control input $\mathbf{u}_k^*$ can be found given the system state (i.e., $\mathbf{x}_k$), providing a closed-form solution to the problem.

**Algorithm 1:** Training Neural Network

1 Let $N = \frac{t_f}{\delta t}$;
2 Select a small positive number $\epsilon$, and a big enough integer $IterMax$;
3 Select $\zeta$ random training samples $\mathbf{x}_{N-1}^{(h)}$, h=$\{1, 2, ..., \zeta\}$ in your region of interest;
4 Guess an initial weight matrix $W_{N-1}^0$;
5 **for** i = 1*: IterMax* **do**
6 Find $W_{N-1}^i$ using (39) with least squares on the entire set of training samples;
7 **if** $\|W_{N-1}^i - W_{N-1}^{i-1}\| \leq \epsilon$ **then**
8 **Break**;
**end**
**end**
9 Set $W_{N-1} = W_{N-1}^i$;
10 **for** k = N-2*: -1: 0* **do**
11 Select $\zeta$ random training samples $\mathbf{x}_k^{(h)}$, h=$\{1, 2, ..., \zeta\}$ in your region of interest;
12 Guess an initial weight matrix $W_k^0$;
13 **for** i = 1*: IterMax* **do**
14 Find $W_k^i$ using (40) with least squares on the entire set of training samples;
15 **if** $\|W_k^i - W_k^{i-1}\| \leq \epsilon$ **then**
16 **Break**;
**end**
**end**
17 Set $W_k = W_k^i$;
**end**

## V. Simulation Results

In this section, a motivating example in which a multiagent system (MAS) of four off-road HEVs that are following a leader is considered. Vehicles are autonomous and connected together through vehicle-to-vehicle communications. The vehicles are assumed identical. Specifications of the environment and vehicles are presented in **Table** A.I in Appendix A. The goal is to form a desired formation, as depicted in Fig. 6, while following the leader whose velocity and position profiles are known and shown in Fig. 7. Following [25], the vehicles' upper-level velocity profiles are shown in Fig. 8. Interested readers are referred to [25] for more details. In this paper, we mainly focus on the lower-level control problem, which deals with powertrain energy management.

The battery power is limited to $-60.5kW \leq P_{batt} \leq 60.5kW$. The initial and the final $SoC$ of all vehicles are set to 60% to have a charge sustaining condition. The simulation time, $t_f$, is 200 sec, and the penalty matrices

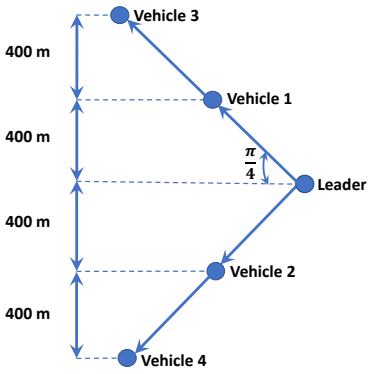


Fig. 6. Desired Formation in the MAS.

are as follows:

$$R = diag([10; 10]) \tag{41}$$
$$S = diag([10^5; 10^5; 10^6; 0; 0]) \tag{42}$$
$$Q = diag([0; 0; 0; 0; 10^2]). \tag{43}$$

Note that the region of interest is selected based on the expected range of states to be visited during the operation of the system, i.e., system constraints [64]. The region of interest in this study is defined as:

$$\Delta x_{min} \leqslant \Delta x(t) \leqslant \Delta x_{max} \tag{44}$$
$$\Delta v_{x,min} \leqslant \Delta v_x(t) \leqslant \Delta v_{x,max} \tag{45}$$
$$SoC_{min} \leqslant SoC(t) \leqslant SoC_{max} \tag{46}$$
$$\Delta T_{d,min} \leqslant \Delta T_d(t) \leqslant \Delta T_{d,max} \tag{47}$$
$$\omega_{e,min} \leqslant \omega_e(t) \leqslant \omega_{e,max} \tag{48}$$

where $diag([a; b])$ is a diagonal matrix with values of $a$ and $b$ on the main diagonal and zero elsewhere. The reason for selecting such $S$ & $Q$ matrices is to minimize $\omega_e$, which correlates with the fuel consumption [49]. Thus, only the corresponding array of $\omega_e$ on $Q$ is set to a nonzero value, i.e., there is no penalty associated with any value for $\Delta x$, $\Delta v_x$, $SoC$, and $\Delta T_d$ in the intermediate steps. Similarly, the S matrix is chosen to enforce the final conditions on $\Delta x$, $\Delta v$, and $SoC$. Note that since $\omega_e$ and $\Delta T_d$ are inherently inputs (before transformation), no desired values are considered for them by setting their corresponding arrays in matrix S to zero. Also, the elements of $\Phi$ function are chosen to be non-repeating polynomials of the form ${x_m}^a {x_n}^b$, where $m, n \in \{1, 2, ..., 5\}$ and $a, b \in \{0, 1, 2\}$ such that $a + b \leq 2$. In addition, the measure of the flexibility for $T_d$ can be constrained by the maximum torque of the engine and the motor at the current speed. For simplicity, the limitations of the flexibilities remain constant [49].

The powertrain control performance using the proposed control method for the first vehicle is shown in Figs. 9-17. The rest of the vehicles behave in a similar manner. To show the efficacy of the "Flexible Driveline Power Demand" concept, the same problem is solved with the "Fixed Driveline Power Demand" scenario (meaning no deviation is allowed for driveline torque after the upper level), and the results of both cases are shown in Figs. 11-17 for comparison.

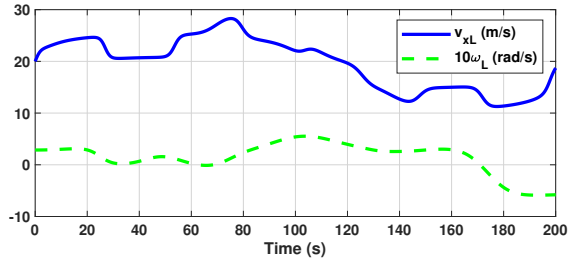


Fig. 7. Leader Linear & Angular Velocity Profile.

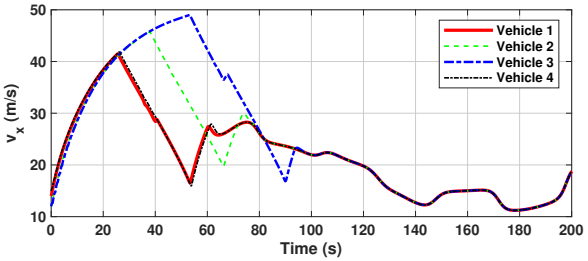


Fig. 8. Upper-Level Velocities for MAS Vehicles.

As can be seen from the simulation results, during the driving cycle considered, $\Delta v$ (the difference between the actual vehicle velocity and the planned velocity from the vehicle-level controller) is negative at the beginning and then rises to be positive at around 60 seconds. This means that the vehicle lags behind the planned vehicle velocity profile (by the vehicle-level controller) initially and then quickly ramps up speed to compensate for the gap in a later phase of the controlled period. This is also reflected by the position deviation $\Delta x$ from the planned trajectory (Fig. 9), which indicates that the vehicle lags behind at the beginning and then gradually catches up. This is because, in the first 25 seconds, the vehicle accelerates quickly (refer to Fig. 8), and therefore, the vehicle-level controller requests a high power demand. But this can overload the engine and cause the powertrain to operate in an inefficient condition. Given the flexibility of power provided by the powertrain control, the powertrain-level controller optimizes the power output by considering the optimal powertrain operating region and outputs less power than requested. This results in an expected instantaneous position deviation in the allowable margin at the beginning. After the high power demand phase is passed, the controller quickly compensates for the deviations in both velocity and longitudinal position towards the end of the driving cycle. Also, note that as we are considering an off-road scenario, having a deviation larger than usual deviations in on-road cases are expected. For instance, refer to [25].

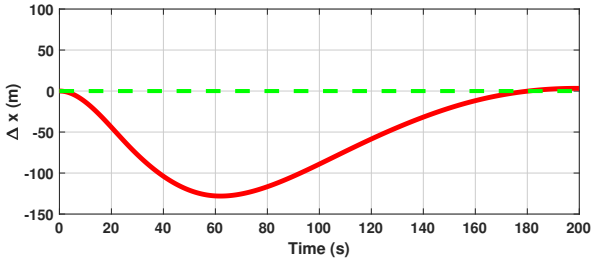


Fig. 9. Position Deviation History for Vehicle 1.

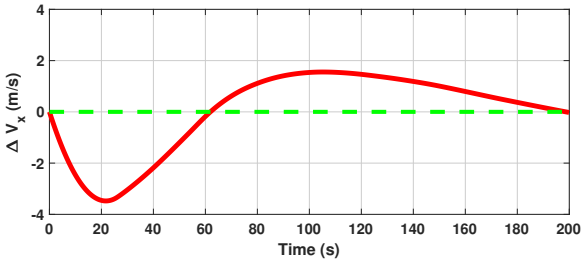


Fig. 10. Velocity Deviation History for Vehicle 1.

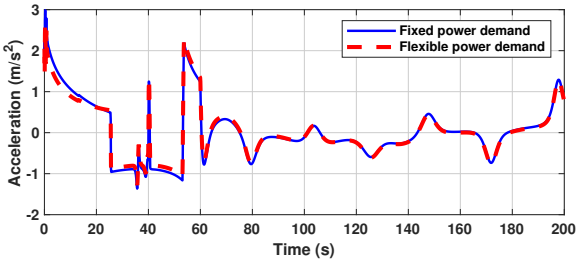


Fig. 11. Acceleration History for Vehicle 1.

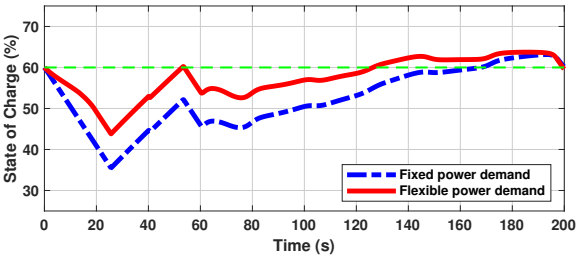


Fig. 12. State of Charge History for Vehicle 1.

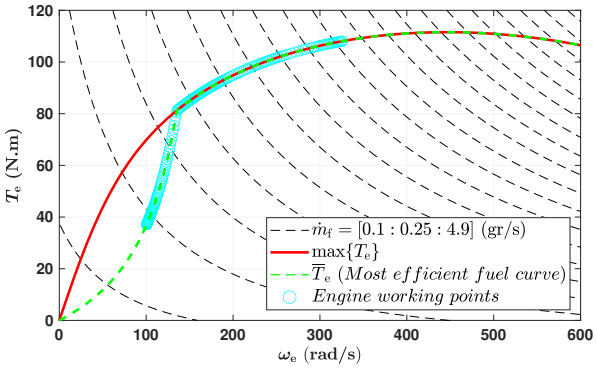


Fig. 13. Engine Working Points.

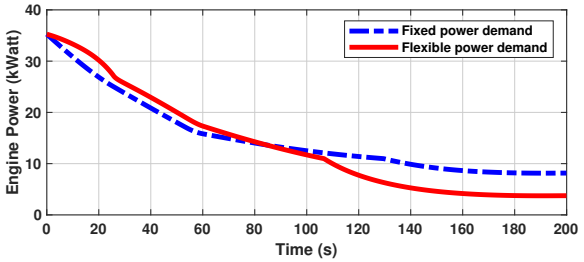


Fig. 14. Engine Power History for Vehicle 1.

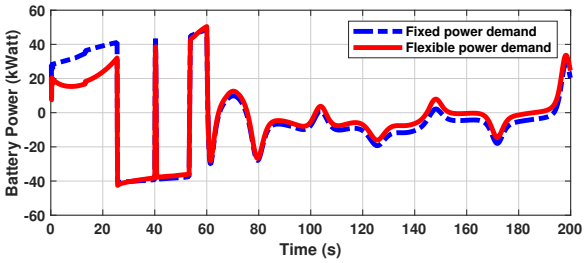


Fig. 15. Battery Power History for Vehicle 1.

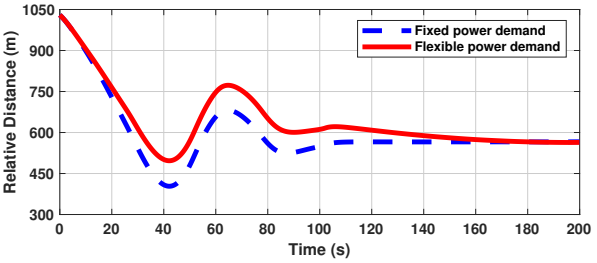


Fig. 16. Relative Distance of Vehicle 1 from the leader.

Flexible power demand has also improved the driveability of the ride. As shown in Fig. (11), the acceleration profile of the vehicle has been smoothed compared to the fixed power demand case, specifically, during the first 50 seconds in which the vehicle initially accelerates quickly (from 0 to 25 s) and then decelerates sharply (from 25 to 50 s). For the rest of the drive cycle, the acceleration is almost the same as the fixed power demand case. Thus, the overall drivability has improved.

During the high power demand phase (first 60 seconds), both the battery and the engine have to operate to supply the power requested by the vehicle. This is evident in Fig. 12, where during the first 25 seconds, the battery state of charge ($SoC$) decreases, indicating that the battery is discharged to supply electrical power. Meanwhile, the power output from the ICE is also at its high end. After passing the high power demand phase, the generator starts to charge the battery, resulting in a rising $SoC$, as shown in Fig. 12. The corresponding engine working points, engine power, and battery power are shown in Figs. 13-15, respectively. The relative distance between Vehicle 1 and

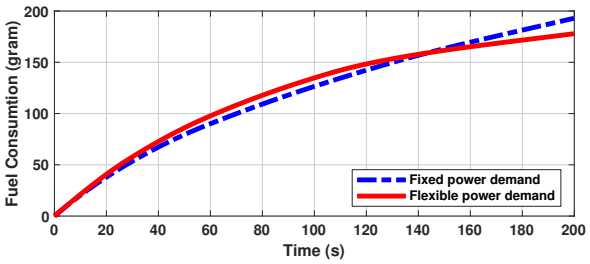


Fig. 17. Fuel Consumption History for Vehicle 1.

the leader is shown in Fig. 16. Considering the desired formation represented in Fig. 6, the desired distance between Vehicle 1 and the leader should be $400\sqrt{2} \approx 565.7(m)$. Starting from the same given initial relative distance, the relative distance in the flexible power demand scenario is more relaxed due to the added degree of freedom to the vehicle dynamics. However, the desired relative distance is met in both scenarios from the last 40 seconds of the drive cycle.

Fuel consumption histories using the fixed power demand strategy and flexible power demand strategy for the drive cycle are shown in Fig. 17. Since the final $SoC$ may not reach exactly the desired value in practical implementations, the fuel consumption compensation method proposed in [65] is used (Eq. (49)) to account for the $SoC$ variation.

$$FC_0 = FC - \sigma \Delta SoC \tag{49}$$

where $FC$, $FC_0$, and $\Delta SoC$ represent the measured fuel consumption, the fuel consumption corresponding to a zero $SoC$ variation, and the final $SoC$ variation, respectively. Also, $\sigma$ is a curve-fitting coefficient that converts $\Delta SoC$ into a corresponding amount of fuel [65]. Comparisons between the compensated fuel consumption using the two strategies for this drive cycle (case 1) and a commonly used drive cycle known as FTP-75 (case 2) for the same time horizon and off-road assumption are shown in Table I.

TABLE I
COMPARISONS OF DIFFERENT ENERGY MANAGEMENT STRATEGIES.

| | Strategy | Initial $SoC(\%)$ | Final $SoC(\%)$ | $FC_0$ (g) |
|---|---|---|---|---|
| Case 1 | Fixed Demand | 60.00 | 60.19 | 192.0 |
| Case 1 | Flexible Demand | 60.00 | 59.62 | 179.7 |
| Case 2 | Fixed Demand | 60.00 | 59.78 | 60.6 |
| Case 2 | Flexible Demand | 60.00 | 59.84 | 52.3 |

This table shows that the concept of the "Flexible Driveline Power Demand" improves the fuel efficiency by close to 6.4 % and 13.7% in case 1 and case 2, respectively.

Finally, the computational efficiency of the proposed algorithm is shown in Fig. 18. Five cases of different durations of the driving cycle of case 1 are presented in the figure, which indicates that the time needed for the controller computation is much less than the duration of the driving cycles. This demonstrates that the proposed controller can be potentially used for real-time solutions.

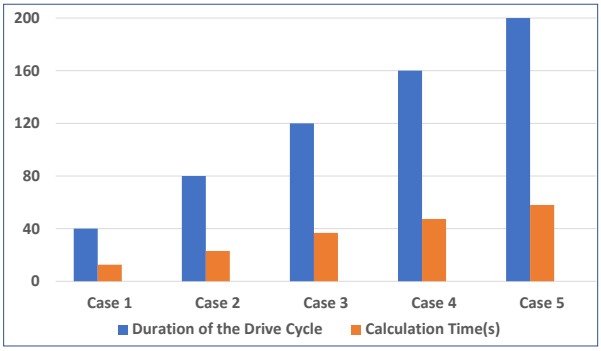


Fig. 18. Computational Time Needed for Driving Cycles of Different Durations.

## VI. Conclusion

This paper studies the powertrain optimal control for an autonomous hybrid electric vehicle. A novel control strategy is explored by taking advantage of a unique feature in the powertrain management of an autonomous HEV, i.e., the instantaneous power generated by the powertrain does not need to strictly follow the power demand from the vehicle motion controller. This feature adds an extra degree of freedom to the optimization problem and can lead to a better fuel economy. Approximate Dynamic Programming is used to solve this optimal control problem with flexible power demand for the first time, and provides a closed-form control solution. Finally, to verify this method, a motivating numerical example of connected HEVs following a leader vehicle in an off-road scenario is presented. In our future work, we will explore the extension of this study to include the engine's shut-off command by means of switched systems [66].

## Appendix A

The vehicles considered in this study are identical. **Table** A.I displays the specifications of the environment and vehicles.

## Acknowledgment

This research was partially supported by the National Science Foundation under Grant No. 1826410. The authors would like to thank the reviewers and Dr. Masood Ghasemi for their time and constructive comments concerning our manuscript.

## References

[1] W. Wang, X. Guo, C. Yang, Y. Zhang, Y. Zhao, D. Huang, and C. Xiang, "A multi-objective optimization energy management strategy for power split hev based on velocity prediction," *Energy*, vol. 238, p. 121714, 2022.

TABLE A.I
ENVIRONMENT SPECIFICATIONS & VEHICLE SYSTEM PARAMETERS

| Parameter | Value | Parameter | Value |
|---|---|---|---|
| m | 1350 kg | $I$ | 1850 kgm$^2$ |
| $I_f$ | 2 kgm$^2$ | $I_r$ | 7 kgm$^2$ |
| $d_f$ | 1.5 m | $d_r$ | 0.9 m |
| r | 0.28 m | $f_\mu$ | 0.007 |
| $\rho$ | 1.225 kgs/m$^3$ | $C_d$ | 0.3 |
| $A_f$ | 2.2 m$^2$ | $k_c$ | 3.9 |
| $r_s$ | 0.030 m | $r_r$ | 0.078 m |
| $\mu_g$ | 0.9 | $\mu_m$ | 0.9 |
| $V_b$ | 330 V | $Q_b$ | 23400 A.s |
| $R_b$ | 0.45 Ω | $\Delta x_{des}(N)$ | 0 m |
| $\Delta v_{x,des}(N)$ | 0 m/s | $SoC_{des}(N)$ | 60 % |
| $\Delta x_{min}$ | -300 m | $\Delta x_{max}$ | 300 m |
| $\Delta v_{x,min}$ | -6 m/s | $\Delta v_{x,max}$ | 6 m/s |
| $SoC_{min}$ | 40 % | $SoC_{max}$ | 70 % |
| $\Delta T_{d,min}$ | -150 N.m | $\Delta T_{d,max}$ | 150 N.m |
| $\omega_{e,min}$ | 50 rad/s | $\omega_{e,max}$ | 450 rad/s |
| $\epsilon$ | 0.05 | $IterMax$ | 10 |
| $\zeta$ | 1000 | | |


[2] J. Liu and H. Peng, "Modeling and control of a power-split hybrid vehicle," *IEEE transactions on control systems technology*, vol. 16, no. 6, pp. 1242–1251, 2008.

[3] Y. L. Murphey, J. Park, L. Kiliaris, M. L. Kuang, M. A. Masrur, A. M. Phillips, and Q. Wang, "Intelligent hybrid vehicle power control—part ii: Online intelligent energy management," *IEEE Transactions on Vehicular Technology*, vol. 62, no. 1, pp. 69–79, 2012.

[4] R. Langari and J.-S. Won, "Intelligent energy management agent for a parallel hybrid vehicle-part i: system architecture and design of the driving situation identification process," *IEEE transactions on vehicular technology*, vol. 54, no. 3, pp. 925–934, 2005.

[5] Z. Chen, C. C. Mi, J. Xu, X. Gong, and C. You, "Energy management for a power-split plug-in hybrid electric vehicle based on dynamic programming and neural networks," *IEEE Transactions on Vehicular Technology*, vol. 63, no. 4, pp. 1567–1580, 2013.

[6] S. Delprat, J. Lauber, T.-M. Guerra, and J. Rimaux, "Control of a parallel hybrid powertrain: optimal control," *IEEE transactions on Vehicular Technology*, vol. 53, no. 3, pp. 872–881, 2004.

[7] G. Buccoliero, P. G. Anselma, S. A. Bonab, G. Belingardi, and A. Emadi, "A new energy management strategy for multimode power-split hybrid electric vehicles," *IEEE Transactions on Vehicular Technology*, vol. 69, no. 1, pp. 172–181, 2019.

[8] B. Sampathnarayanan, S. Onori, and S. Yurkovich, "An optimal regulation strategy with disturbance rejection for energy management of hybrid electric vehicles," *Automatica*, vol. 50, no. 1, pp. 128–140, 2014.

[9] A. A. Malikopoulos, "Supervisory power management control algorithms for hybrid electric vehicles: A survey," *IEEE Transactions on intelligent transportation systems*, vol. 15, no. 5, pp. 1869–1885, 2014.

[10] E. Silvas, T. Hofman, N. Murgovski, L. P. Etman, and M. Steinbuch, "Review of optimization strategies for system-level design in hybrid electric vehicles," *IEEE Transactions on Vehicular Technology*, vol. 66, no. 1, pp. 57–70, 2016.

[11] X. Zeng and J. Wang, "A parallel hybrid electric vehicle energy management strategy using stochastic model predictive control with road grade preview," *IEEE Transactions on Control Systems Technology*, vol. 23, no. 6, pp. 2416–2423, 2015.

[12] J. T. Kessels, M. W. Koot, P. P. Van Den Bosch, and D. B. Kok, "Online energy management for hybrid electric vehicles," *IEEE Transactions on vehicular technology*, vol. 57, no. 6, pp. 3428–3440, 2008.

[13] Y. Yang, H. Pei, X. Hu, Y. Liu, C. Hou, and D. Cao, "Fuel economy optimization of power split hybrid vehicles: A rapid dynamic programming approach," *Energy*, vol. 166, pp. 929–938, 2019.

[14] L. V. Pérez, G. R. Bossio, D. Moitre, and G. O. García, "Optimization of power management in an hybrid electric vehicle using dynamic programming," *Mathematics and Computers in Simulation*, vol. 73, no. 1-4, pp. 244–254, 2006.

[15] N. Jalil, N. A. Kheir, and M. Salman, "A rule-based energy management strategy for a series hybrid vehicle," in *Proceedings of the 1997 American Control Conference (Cat. No. 97CH36041)*, vol. 1. IEEE, 1997, pp. 689–693.

[16] B. Škugor, J. Deur, M. Cipek, and D. Pavković, "Design of a power-split hybrid electric vehicle control system utilizing a rule-based controller and an equivalent consumption minimization strategy," *Proceedings of the Institution of Mechanical Engineers, Part D: Journal of Automobile Engineering*, vol. 228, no. 6, pp. 631–648, 2014.

[17] G. Paganelli, S. Delprat, T.-M. Guerra, J. Rimaux, and J.-J. Santin, "Equivalent consumption minimization strategy for parallel hybrid powertrains," in *Vehicular Technology Conference. IEEE 55th Vehicular Technology Conference. VTC Spring 2002 (Cat. No. 02CH37367)*, vol. 4. IEEE, 2002, pp. 2076–2081.

[18] S. Nazari, R. Middleton, J. Siegel, and A. Stefanopoulou, "Equivalent consumption minimization strategy for a power split supercharger," *SAE Technical Paper, Tech. Rep*, pp. 01–1207, 2019.

[19] S. G. Li, S. Sharkh, F. C. Walsh, and C.-N. Zhang, "Energy and battery management of a plug-in series hybrid electric vehicle using fuzzy logic," *IEEE Transactions on Vehicular Technology*, vol. 60, no. 8, pp. 3571–3585, 2011.

[20] N. J. Schouten, M. A. Salman, and N. A. Kheir, "Fuzzy logic control for parallel hybrid vehicles," *IEEE transactions on control systems technology*, vol. 10, no. 3, pp. 460–468, 2002.

[21] C. Xiang, F. Ding, W. Wang, and W. He, "Energy management of a dual-mode power-split hybrid electric vehicle based on velocity prediction and nonlinear model predictive control," *Applied energy*, vol. 189, pp. 640–653, 2017.

[22] H. A. Borhan, C. Zhang, A. Vahidi, A. M. Phillips, M. L. Kuang, and S. Di Cairano, "Nonlinear model predictive control for power-split hybrid electric vehicles," in *49th IEEE Conference on Decision and Control (CDC)*. IEEE, 2010, pp. 4890–4895.

[23] J. Wu, H. He, J. Peng, Y. Li, and Z. Li, "Continuous reinforcement learning of energy management with deep q network for a power split hybrid electric bus," *Applied energy*, vol. 222, pp. 799–811, 2018.

[24] Y. Li, H. He, A. Khajepour, H. Wang, and J. Peng, "Energy management for a power-split hybrid electric bus via deep reinforcement learning with terrain information," *Applied Energy*, vol. 255, p. 113762, 2019.

[25] M. Ghasemi and X. Song, "Powertrain energy management for autonomous hybrid electric vehicles with flexible driveline power demand," *IEEE Transactions on Control Systems Technology*, vol. 27, no. 5, pp. 2229–2236, 2018.

[26] S. J. Anderson, S. C. Peters, T. E. Pilutti, and K. Iagnemma, "An optimal-control-based framework for trajectory planning, threat assessment, and semi-autonomous control of passenger vehicles in hazard avoidance scenarios," *International Journal of Vehicle Autonomous Systems*, vol. 8, no. 2-4, pp. 190–216, 2010.

[27] G. Foderaro, S. Ferrari, and T. A. Wettergren, "Distributed optimal control for multi-agent trajectory optimization," *Automatica*, vol. 50, no. 1, pp. 149–154, 2014.

[28] P. Jantapremjit and P. A. Wilson, "Control and guidance for homing and docking tasks using an autonomous underwater vehicle," in *2007 IEEE/RSJ International Conference on Intelligent Robots and Systems*. IEEE, 2007, pp. 3672–3677.

[29] J. Ma, Y. Zheng, and L. Wang, "Lqr-based optimal topology of leader-following consensus," *International Journal of Robust and Nonlinear Control*, vol. 25, no. 17, pp. 3404–3421, 2015.

[30] H. Zhang, T. Feng, G.-H. Yang, and H. Liang, "Distributed cooperative optimal control for multiagent systems on directed graphs: An inverse optimal approach," *IEEE Transactions on Cybernetics*, vol. 45, no. 7, pp. 1315–1326, 2014.

[31] H. Zhang, J. Zhang, G.-H. Yang, and Y. Luo, "Leader-based optimal coordination control for the consensus problem of multiagent differential games via fuzzy adaptive dynamic programming," *IEEE Transactions on Fuzzy Systems*, vol. 23, no. 1, pp. 152–163, 2014.

[32] M. A. M. Zulkefli, J. Zheng, Z. Sun, and H. X. Liu, "Hybrid powertrain optimization with trajectory prediction based on inter-vehicle-communication and vehicle-infrastructure-integration," *Transportation Research Part C: Emerging Technologies*, vol. 45, pp. 41–63, 2014.

[33] S. J. Kim, K.-S. Kim, and D. Kum, "Feasibility assessment and design optimization of a clutchless multimode parallel hybrid electric powertrain," *IEEE/ASME Transactions on Mechatronics*, vol. 21, no. 2, pp. 774–786, 2015.

[34] A. Panday and H. O. Bansal, "A review of optimal energy management strategies for hybrid electric vehicle," *International Journal of Vehicular Technology*, vol. 2014, 2014.

[35] N. Kim, S. W. Cha, and H. Peng, "Optimal equivalent fuel consumption for hybrid electric vehicles," *IEEE Transactions on Control Systems Technology*, vol. 20, no. 3, pp. 817–825, 2011.

[36] H. Kim and D. Kum, "Comprehensive design methodology of input-and output-split hybrid electric vehicles: In search of optimal configuration," *IEEE/ASME Transactions on Mechatronics*, vol. 21, no. 6, pp. 2912–2923, 2016.

[37] N. Kim, A. Rousseau, and D. Lee, "A jump condition of pmp-based control for phevs," *Journal of Power Sources*, vol. 196, no. 23, pp. 10 380–10 386, 2011.

[38] C. Atkinson, A. Lewis, A. Salvia, and G. Vishwanathan, "Powertrain innovations for connected and autonomous vehicles," in *Proc. Powertrain Innov. Workshop, Adv. Res. Projects Agency-Energy*, 2015, pp. 1–8.

[39] Y. Kim, M. Figueroa-Santos, N. Prakash, S. Baek, J. B. Siegel, and D. M. Rizzo, "Co-optimization of speed trajectory and power management for a fuel-cell/battery electric vehicle," *Applied Energy*, vol. 260, p. 114254, 2020.

[40] G. Heppeler, M. Sonntag, and O. Sawodny, "Fuel efficiency analysis for simultaneous optimization of the velocity trajectory and the energy management in hybrid electric vehicles," *IFAC Proceedings Volumes*, vol. 47, no. 3, pp. 6612–6617, 2014.

[41] D. Chen, M. Huang, A. Stefanopoulou, and Y. Kim, "A receding-horizon framework for co-optimizing the velocity and power-split of automated plug-in hybrid electric vehicles," *ASME Letters in Dynamic Systems and Control*, vol. 1, no. 4, 2021.

[42] B. Chen, S. A. Evangelou, and R. Lot, "Series hybrid electric vehicle simultaneous energy management and driving speed optimization," *IEEE/ASME Transactions on Mechatronics*, vol. 24, no. 6, pp. 2756–2767, 2019.

[43] G. Ma, M. Ghasemi, and X. Song, "Integrated powertrain energy management and vehicle coordination for multiple connected hybrid electric vehicles," *IEEE Transactions on Vehicular Technology*, vol. 67, no. 4, pp. 2893–2899, 2017.

[44] H. Zheng, J. Wu, W. Wu, and Y. Wang, "Integrated motion and powertrain predictive control of intelligent fuel cell/battery hybrid vehicles," *IEEE Transactions on Industrial Informatics*, vol. 16, no. 5, pp. 3397–3406, 2019.

[45] X. Pan, B. Chen, and S. A. Evangelou, "Optimal vehicle following strategy for joint velocity and energy management control of series hybrid electric vehicles," *IFAC-PapersOnLine*, vol. 53, no. 2, pp. 14 161–14 166, 2020.

[46] L. Zhang, X. Ye, X. Xia, and F. Barzegar, "A real-time energy management and speed controller for an electric vehicle powered by a hybrid energy storage system," *IEEE Transactions on Industrial Informatics*, vol. 16, no. 10, pp. 6272–6280, 2020.

[47] L. Zhao, A. I. Mahbub, and A. A. Malikopoulos, "Optimal vehicle dynamics and powertrain control for connected and automated vehicles," in *2019 IEEE conference on control technology and applications (CCTA)*. IEEE, 2019, pp. 33–38.

[48] A. Mahbub and A. A. Malikopoulos, "Concurrent optimization of vehicle dynamics and powertrain operation using connectivity and automation," *arXiv preprint arXiv:1911.03475*, 2019.

[49] F. Zhang, X. Hu, R. Langari, L. Wang, Y. Cui, and H. Pang, "Adaptive energy management in automated hybrid electric vehicles with flexible torque request," *Energy*, vol. 214, p. 118873, 2021.

[50] M. Sánchez, S. Delprat, and T. Hofman, "Energy management of hybrid vehicles with state constraints: A penalty and implicit hamiltonian minimization approach," *Applied Energy*, vol. 260, p. 114149, 2020.

[51] Q. Jiang, F. Ossart, and C. Marchand, "Comparative study of real-time hev energy management strategies," *IEEE Transactions on Vehicular Technology*, vol. 66, no. 12, pp. 10 875–10 888, 2017.

[52] L. Serrao, S. Onori, and G. Rizzoni, "Ecms as a realization of pontryagin's minimum principle for hev control," in *2009 American control conference*. IEEE, 2009, pp. 3964–3969.

[53] N. W. Kim, D. H. Lee, C. Zheng, C. Shin, H. Seo, and S. W. Cha, "Realization of pmp-based control for hybrid electric vehicles in a backward-looking simulation," *International Journal of Automotive Technology*, vol. 15, no. 4, pp. 625–635, 2014.

[54] D. E. Kirk, *Optimal control theory: an introduction*. Englewood Cliffs, NJ, USA: Prentice-Hall, 1970, pp. 343–356.

[55] S. Han, F. Zhang, and J. Xi, "A real-time energy management strategy based on energy prediction for parallel hybrid electric vehicles," *IEEE access*, vol. 6, pp. 70 313–70 323, 2018.

[56] M. Ghasemi and X. Song, "Control and powertrain management for multi-autonomous hybrid vehicles," *Journal of Dynamic Systems, Measurement, and Control*, vol. 141, no. 7, 2019.

[57] J. Pei, Y. Su, D. Zhang, Y. Qi, and Z. Leng, "Velocity forecasts using a combined deep learning model in hybrid electric vehicles with v2v and v2i communication," *Science China Technological Sciences*, vol. 63, no. 1, pp. 55–64, 2020.

[58] Y. Zhang, L. Chu, Z. Fu, N. Xu, C. Guo, X. Zhang, Z. Chen, and P. Wang, "Optimal energy management strategy for parallel plug-in hybrid electric vehicle based on driving behavior analysis and real time traffic information prediction," *Mechatronics*, vol. 46, pp. 177–192, 2017.

[59] N. Kim, S. Cha, and H. Peng, "Optimal control of hybrid electric vehicles based on pontryagin's minimum principle," *IEEE Transactions on control systems technology*, vol. 19, no. 5, pp. 1279–1287, 2010.

[60] S. Stockar, V. Marano, G. Rizzoni, and L. Guzzella, "Optimal control for plug-in hybrid electric vehicle applications," in *Proceedings of the 2010 American control conference*. IEEE, 2010, pp. 5024–5030.

[61] H. Borhan, A. Vahidi, A. M. Phillips, M. L. Kuang, I. V. Kolmanovsky, and S. Di Cairano, "Mpc-based energy management of a power-split hybrid electric vehicle," *IEEE Transactions on Control Systems Technology*, vol. 20, no. 3, pp. 593–603, 2011.

[62] A. Heydari and S. N. Balakrishnan, "Fixed-final-time optimal tracking control of input-affine nonlinear systems," *Neurocomputing*, vol. 129, pp. 528–539, 2014.

[63] T. Sardarmehni and X. Song, "Sub-optimal control of autonomous wheel loader with approximate dynamic programming," in *ASME 2019 Dynamic Systems and Control Conference*. American Society of Mechanical Engineers Digital Collection, 2019.

[64] A. Heydari, "Stability analysis of optimal adaptive control using value iteration with approximation errors," *IEEE Transactions on Automatic Control*, vol. 63, no. 9, pp. 3119–3126, 2018.

[65] S. Onori, L. Serrao, and G. Rizzoni, "Hybrid electric vehicles: Energy management strategies," 2016.

[66] T. Sardarmehni and X. Song, "Sub-optimal tracking in switched systems with fixed final time and fixed mode sequence using reinforcement learning," *Neurocomputing*, vol. 420, pp. 197–209, 2021.